Complex dynamics in a short annular container with rotating bottom and inner cylinder

By J. M. LOPEZ[1], F. MARQUES[2] AND J. SHEN[3]

[1]Department of Mathematics and Statistics, Arizona State University, Tempe, AZ 85287, USA

[2]Departament de Física Aplicada, Universitat Politècnica de Catalunya, Jordi Girona Salgado s/n, Mòdul B4 Campus Nord, 08034 Barcelona, Spain

[3]Department of Mathematics, Purdue University, West Lafayette, IN 47907, USA

The nonlinear dynamics of the flow in a short annulus driven by the rotation of the inner cylinder and bottom endwall is considered. The shortness of the annulus enhances the role of mode competition. For aspect ratios greater than about 3, the flow dynamics are dominated by a centrifugal instability as the rotating inner cylinder imparts angular momentum to the adjacent fluid, resulting in a three-cell state; the cells are analoguous to Taylor–Couette vortices. For aspect ratios less than about 2.8, the dynamics are dominated by the boundary layer on the bottom rotating endwall that is turned by the stationary outer cylinder to produce an internal shear layer that is azimuthally unstable via Hopf bifurcations. For intermediate aspect ratios, the competition between these instability mechanisms leads to very complicated dynamics, including homoclinic and heteroclinic phenomena. The dynamics are organized by a codimension-two fold-Hopf bifurcation, where modes due to both instability mechanisms bifurcate simultaneously. The dynamics are explored using a three-dimensional Navier–Stokes solver, which is also implemented in a number of invariant subspaces in order to follow some unstable solution branches and obtain a fairly complete bifurcation diagram of the mode competitions.

1. Introduction

In a recent experimental study, Mullin & Blohm (2001) have explored the primary instabilities and mode competition in flow inside an annulus whose bottom endwall rotates with the inner cylinder and the top endwall remains stationary with the outer cylinder. In that study, the focus was on the case of a relatively short annulus where there are states with either one or three cells, A_1 and A_3 states, respectively, and a regime where these two states compete. The primary competition between the two states results in hysteretic behaviour as parameters are varied. In the experiments, the radius ratio of the cylinders was held fixed and only two parameters were varied: the annulus aspect ratio and the inner cylinder rotation rate. In this two-parameter space, the hysteresis manifests itself as a pair of saddle-node (fold) bifurcation curves which meet at a codimension-2 cusp point. The associated bifurcations were found to be steady and axisymmetric, and excellent agreement between nonlinear steady axisymmetric computations and the experiments was observed. Figure 1 is a reproduction of their figure 7, summarizing their findings.

The experiments of Mullin & Blohm (2001) also revealed interesting time-dependent behaviour in which the $SO(2)$ symmetry (invariance to arbitrary rotations about the
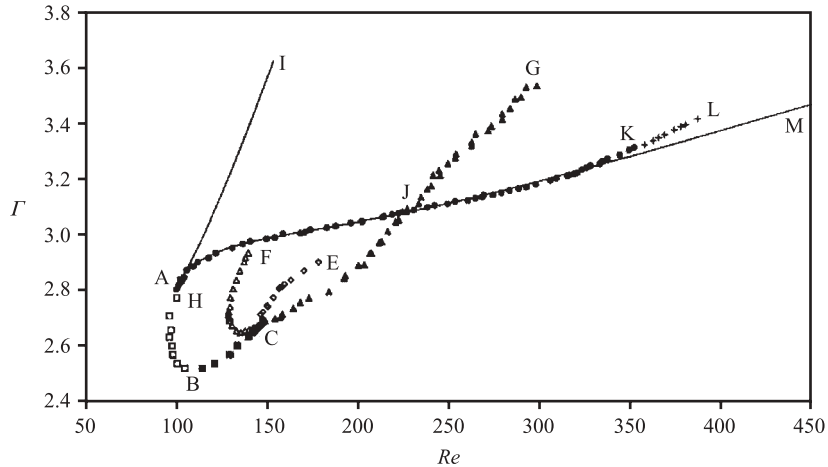
FIGURE 1. Reproduction of figure 7 from Mullin & Blohm (2001); the curve HL is the path of saddle-nodes for three cells, HI that for a single cell, and H corresponds to a cusp point; the curves ABC and CG correspond to two different Hopf bifurcations, the point C is the double Hopf bifurcation point. CE and CF are curves of Neimark–Sacker bifurcations. The symbols represent experimentally determined points, and the solid curves HM and HI were numerically determined.

annulus axis) was broken via supercritical Hopf bifurcations. They also documented dynamics associated with a double Hopf bifurcation. The resulting non-axisymmetric time-periodic states were beyond the capabilities of their numerics, and many open questions remained, such as what is the spatial structure of the three-dimensional states, and what happens to these in the parameter regimes where the A_1 and A_3 states compete i.e. in the hysteretic (fold) region? In this paper, we use a three-dimensional Navier–Stokes solver to address these questions and to further explore the nonlinear dynamics associated with the observed double Hopf bifurcation. Mullin & Blohm (2001) did not report on the specific nature of the unsteady states (other than to give the frequency and amplitude of the periodic variations in the radial velocity at a point). Our numerics have revealed that the two Hopf bifurcations are symmetry-breaking to rotating waves with azimuthal wavenumbers 1 (RW_1) and 2 (RW_2). Although the spatial wavenumbers are in a 1:2 ratio, the double Hopf bifurcation is non-resonant as the associated precession frequencies of the rotating waves at the bifurcation (i.e. the two critical pairs of complex-conjugate eigenvalues) are not in a 1:2 ratio. Hence the double Hopf bifurcation, even though it is taking place in an $SO(2)$-equivariant system, has the generic normal form (see the Appendix in Marques, Lopez & Shen 2002 for details). Detailed analyses of double Hopf bifurcations in fluid dynamics are not very common. We have also unveiled a pair of codimension-2 fold-Hopf bifurcations and associated with one of these a global bifurcation that results from the interaction between a two-torus bifurcating from one of the rotating waves, and two (unstable) steady states in the fold from the cusp bifurcation. Cyclic-fold bifurcations (saddle-node bifurcations for limit cycles) have also been found nearby. We believe that these phenomena are novel in fluid dynamics, as is a detailed exploration of how their associated dynamics are all interconnected.
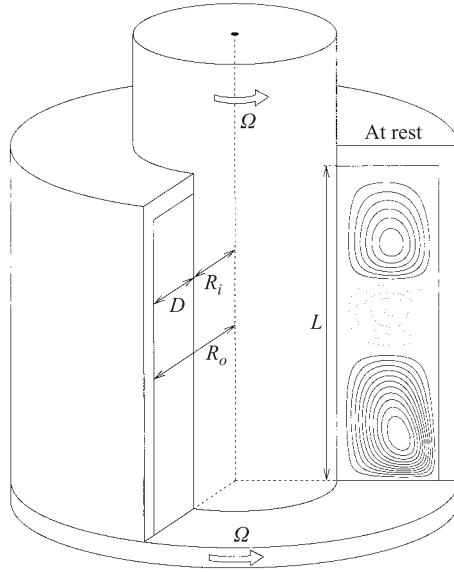
FIGURE 2. Schematic of the flow geometry, with an insert showing the streamlines (solid are positive and dashed are negative contours of the streamfunction) in an (r, z) meridional section for a three-cell steady axisymmetric solution at $Re = 124.5$ and $\Gamma = 3.10$.

2. Navier–Stokes equations and the numerical scheme

We consider an incompressible flow confined in an annulus of inner radius R_i and outer radius R_o and length L, driven by the constant rotation of the inner cylinder and bottom endwall at Ω rad s^{-1} while the outer cylinder and top endwall remain at rest. The system is non-dimensionalized using the gap, $D = R_o - R_i$, as the length scale and the diffusive time across the gap, D^2/ν, as the time scale (where ν is the fluid's kinematic viscosity). The equations governing the flow are the Navier-Stokes equations together with initial and boundary conditions. In cylindrical coordinates, (r, θ, z), we denote the non-dimensional velocity vector and pressure by $\boldsymbol{u} = (u, v, w)^T$ and p, respectively. Keeping the radius ratio fixed at $\eta = R_i/R_o = 0.5$, we consider the dynamics as the other two governing parameters are varied. These parameters are

$$\text{Reynolds number:} \quad Re = \Omega D R_i/\nu,$$
$$\text{annulus aspect ratio:} \quad \Gamma = L/D.$$

A schematic of the flow geometry, with an insert showing the streamlines for a three-cell steady axisymmetric solution at $Re = 124.5$, $\Gamma = 3.10$ is shown in figure 2.

The non-dimensional Navier–Stokes equations in velocity–pressure formulation are

$$\left.\begin{aligned}
\partial_t u + \text{adv}_r &= -\partial_r p + \left(\Delta u - \frac{1}{r^2}u - \frac{2}{r^2}\partial_\theta v \right), \\
\partial_t v + \text{adv}_\theta &= -\partial_\theta p + \left(\Delta v - \frac{1}{r^2}v + \frac{2}{r^2}\partial_\theta u \right), \\
\partial_t w + \text{adv}_z &= -\partial_z p + \Delta w,
\end{aligned}\right\} \tag{2.1}$$

$$\frac{1}{r}\partial_r(ru) + \frac{1}{r}\partial_\theta v + \partial_z w = 0, \tag{2.2}$$

where

$$\Delta = \partial_r^2 + \frac{1}{r}\partial_r + \frac{1}{r^2}\partial_\theta^2 + \partial_z^2 \tag{2.3}$$

is the Laplace operator in cylindrical coordinates and

$$\left.\begin{aligned}
\mathrm{adv}_r &= u\partial_r u + \frac{v}{r}\partial_\theta u + w\partial_z u - \frac{v^2}{r}, \\
\mathrm{adv}_\theta &= u\partial_r v + \frac{v}{r}\partial_\theta v + w\partial_z v - \frac{uv}{r}, \\
\mathrm{adv}_z &= u\partial_r w + \frac{v}{r}\partial_\theta w + w\partial_z w.
\end{aligned}\right\} \tag{2.4}$$

The boundary conditions on all walls are no-slip. Specifically,

$$\begin{aligned}
&\text{stationary outer cylinder}\,(r = r_o): &&u = v = w = 0. \\
&\text{rotating inner cylinder}\,(r = r_i): &&u = w = 0, v = Re. \\
&\text{stationary top endwall}\,(z = \Gamma): &&u = v = w = 0. \\
&\text{rotating bottom endwall}\,(z = 0): &&u = w = 0, v = Re\,r/r_i.
\end{aligned}$$

The annular region consists of $r \in [r_i, r_o] = [\eta/(1 - \eta), 1/(1 - \eta)]$, $z \in [0, \Gamma]$, $\theta \in [0, 2\pi]$. The discontinuities in these ideal boundary conditions at $(r = r_i, z = \Gamma)$ and $(r = r_o, z = 0)$ physically correspond to small but finite gaps between the rotating (stationary) cylinder and the stationary (rotating) endwall. For an accurate use of spectral techniques, a regularization of these discontinuities is implemented of the form:

$$\text{stationary top endwall:} \quad u = w = 0, v = Re \exp\left[-\left(\frac{r - r_i}{\epsilon}\right)^2\right],$$

$$\text{rotating bottom endwall:} \quad u = w = 0, v = Re\,\frac{r}{r_i}\left[1 - \exp\left[-\left(\frac{r_o - r}{\epsilon}\right)^2\right]\right],$$

where ϵ is a small parameter that mimics the small gaps (we have used $\epsilon = 0.005$). The use of $\epsilon \neq 0$ regularizes the otherwise discontinuous boundary conditions. See Lopez & Shen (1998) for further details of the use of this regularization in a spectral code.

Note that in addition to the nonlinear coupling, the velocity components (u, v) are also coupled by the linear operators. Following Orszag & Patera (1983), we introduce a new set of complex functions

$$u_+ = u + \mathrm{i}v, \quad u_- = u - \mathrm{i}v, \tag{2.5}$$

so that

$$u = \frac{1}{2}(u_+ + u_-), \quad v = \frac{1}{2\mathrm{i}}(u_+ - u_-). \tag{2.6}$$

The Navier-Stokes equations (2.1)–(2.2) can then be written using (u_+, u_-, w, p) as

$$\left.\begin{aligned}
\partial_t u_+ + \mathrm{adv}_+ &= -\left(\partial_r + \frac{\mathrm{i}}{r}\partial_\theta\right)p + \left(\Delta - \frac{1}{r^2} + \frac{2\mathrm{i}}{r^2}\partial_\theta\right)u_+, \\
\partial_t u_- + \mathrm{adv}_- &= -\left(\partial_r - \frac{\mathrm{i}}{r}\partial_\theta\right)p + \left(\Delta - \frac{1}{r^2} - \frac{2\mathrm{i}}{r^2}\partial_\theta\right)u_-, \\
\partial_t w + \mathrm{adv}_z &= -\partial_z p + \Delta w,
\end{aligned}\right\} \tag{2.7}$$

$$\left(\partial_r + \frac{1}{r}\right)(u_+ + u_-) - \frac{\mathrm{i}}{r}\partial_\theta(u_+ - u_-) + 2\partial_z w = 0, \tag{2.8}$$

where we have denoted

$$\mathrm{adv}_\pm = \mathrm{adv}_r \pm \mathrm{i}\,\mathrm{adv}_\theta. \tag{2.9}$$

The main difficulty in numerically solving the above equations is due to the fact that the velocity vector and the pressure are coupled through the continuity equation. An efficient way to overcome this difficulty is to use a so-called projection scheme originally proposed by Chorin (1968) and Temam (1969). Here, we use a stiffly stable semi-implicit second-order projection scheme, where the linear terms are treated implicitly while the nonlinear terms are explicit (see Lopez & Shen 1998; Lopez, Marques & Shen 2002, for more details). For the space variables, we use a Legendre–Fourier approximation. More precisely, the azimuthal direction is discretized using a Fourier expansion with $k + 1$ modes corresponding to azimuthal wavenumbers $m = 0, 1, 2, \ldots k/2$, while the axial and radial directions are discretized with a Legendre expansion. With the above discretization, one only needs to solve, at each time step, a Poisson-like equation for each of the velocity components and for pressure. These Poisson-like equations are solved using the spectral–Galerkin method presented in Shen (1994, 1997).

The spectral convergence of the code in the radial and axial directions has already been extensively described in Lopez & Shen (1998) for $m = 0$; the convergence properties in these directions are not affected by $m \neq 0$. For the convergence in azimuth, we note that the modes of instability being investigated here are to rotating waves with azimuthal wavesnumbers 1 or 2, and near the symmetry-breaking bifurcation, the energy in the harmonics is small and so it is sufficient to capture the symmetry breaking using a very small number of azimuthal modes. All the results presented here have 48 and 64 Legendre modes in the radial and axial directions, respectively, and 7 Fourier modes in θ; the time-step is $\delta t = 5 \times 10^{-4}$.

3. Results

3.1. *The steady axisymmetric states*

In this paper, we shall consider the parameter regime $Re \in [100, 200]$, $\Gamma \in [2.5, 3.25]$ and $\eta = 0.5$, corresponding to the regime where Mullin & Blohm (2001) reported interesting dynamics. For $Re = 100$ and low Γ, the flow consists of a single meridional cell, driven essentially by the rotation of the bottom endwall. A rotating-endwall boundary layer is quickly established (within about one rotation) that advects fluid radially outwards. The stationary outer cylinder turns this swirling flow into the axial direction and the stationary top endwall turns it in towards the inner cylinder. During this part of the motion, the fluid dissipates angular momentum that it had acquired in the rotating-endwall boundary layer, but as it flows down past the rotating inner cylinder it re-acquires more angular momentum.

As the length of the cylinders is increased (i.e. increasing Γ), at fixed Re, the rotating inner cylinder begins to play a more important role in the driving of the flow. In the limit $\Gamma \to \infty$, the classical Taylor–Couette flow is approached, where the flow acquires angular momentum in the inner-cylinder boundary layer. This leads to a centrifugally unstable distribution of angular momentum, and a series of counter-rotating toroidal cells that redistribute the angular momentum result. These toroidal cells, in the absence of endwall effects, have roughly square cross-section. For our

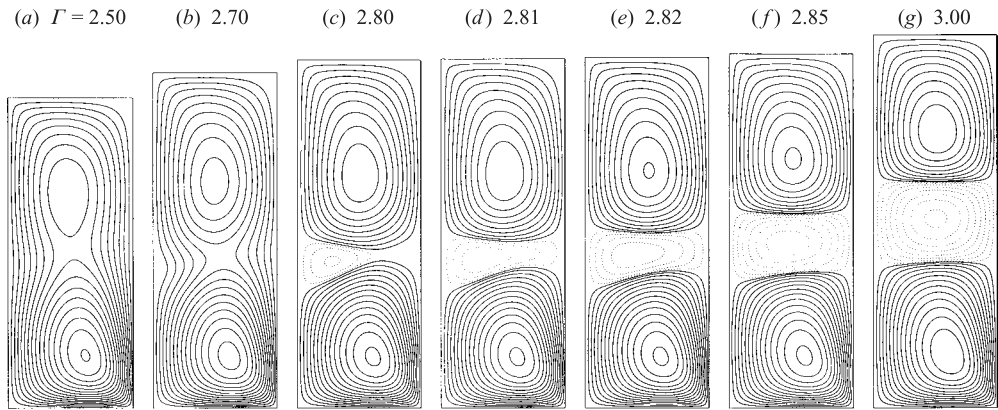(a) $\Gamma = 2.50$ (b) 2.70 (c) 2.80 (d) 2.81 (e) 2.82 (f) 2.85 (g) 3.00

FIGURE 3. Streamlines of the steady axisymmetric solutions for $Re = 100$ and Γ as indicated.

problem, endwall effects are prevalent. Nevertheless, as Γ approaches 3, the flow undergoes a transition from the single meridional overturning cell structure to a three-cell structure with the middle cell counter-rotating (in the meridional plane) compared to the other two. At low Re, this transition from a one-cell (A_1) state to a three-cell (A_3) state is smooth and non-hysteretic. Figure 3 shows the streamlines of the steady axisymmetric states at $Re = 100$ as Γ is varied between 2.50 and 3.00. At Γ between about 2.7 and 2.8, the boundary layer on the rotating inner cylinder separates and a small weak separation bubble forms. The flow near the separation point advects flow with high angular momentum into the interior. As Γ is increased above 2.8, the separation bubble extends further into the interior, although its axial extent remains small. At about $\Gamma = 2.81$, the separation streamline extends to the stationary outer cylinder where it re-attaches; at the outer cylinder at slightly lower z the boundary layer also separates and attaches at the inner cylinder, and a three-cell state is established. With further increase in Γ, the weak middle cell strengthens and grows in axial extent, as seen in figure 3(g) for $\Gamma = 3.0$.

At slightly higher Re, the above transition is no longer smooth. By $Re = 105$, there is a multiplicity of states over a small range of $\Gamma \in (2.8635, 2.8665)$. The two limits in Γ correspond to saddle-node bifurcation points at $Re = 105$. Figure 4 shows a schematic view of the surface of steady solutions. The saddle-node bifurcation curves are labelled S_1 and S_3, and they meet at a cusp point. The hysteresis region is bounded by the curves S_1 and S_3, and in this region A_1 and A_3 are stable and coexist, and there also exists an unstable mid-branch A_m, indicated by a dashed line in the figure.

For ease of presentation, we shall refer to these saddle-node bifurcations, S_1 and S_3, as representing jumps between the A_1 state and the A_3 state, and the A_3 state and the A_1 state, respectively. However, the solution near the saddle-node bifurcation S_1 at the higher Γ value (that is continuous with the solution at much lower Γ) is not strictly a one-cell structure, but rather has already undergone the boundary layer separation on the inner cylinder and the separation streamline has re-attached on the outer cylinder, thus forming an outward jet of angular momentum emanating from the inner cylinder. Figures 5(a) and 5(b) show streamlines of two co-existing stable steady axisymmetric states at the same parameter values ($Re = 105$, $\Gamma = 2.865$); we denote the state depicted in part (a) of the figure as an A_1 state as it is continuous (with decreasing Γ and fixed Re) with the one-cell states at lower Γ, and the state in part (b) is clearly the A_3 state. At higher Re, the range of hysteresis in Γ (i.e. the
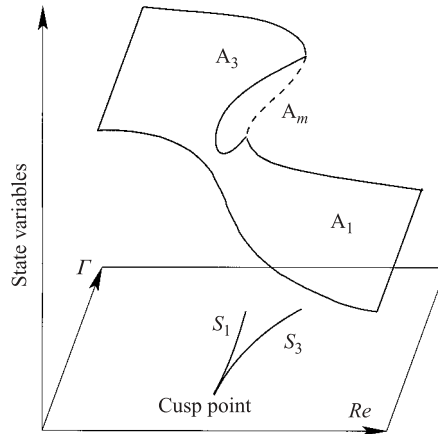
FIGURE 4. Schematic of the cusp bifurcation point where the two saddle-node curves, S_1 and S_3, meet. The stable solutions A_1 and A_3 coexist inside the cusp, along with the unstable mid-branch solution A_m (dashed line).
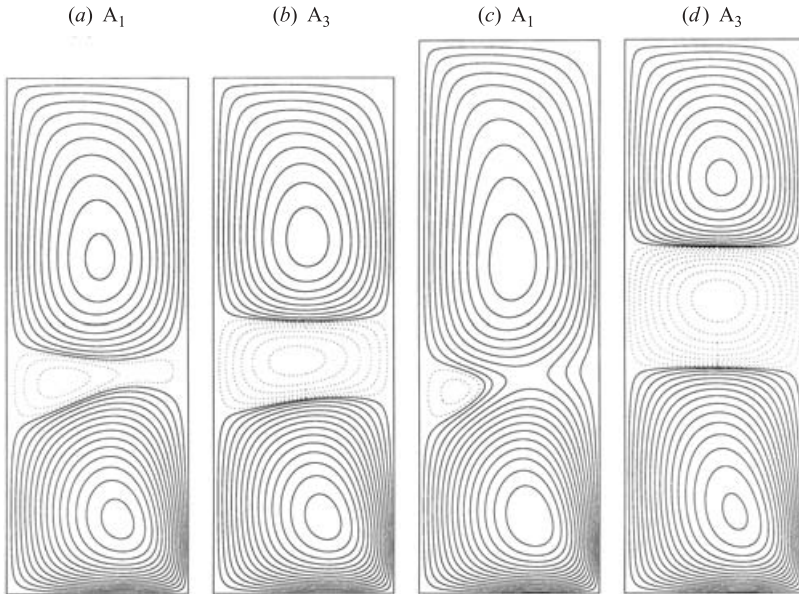

(*a*) A_1 (*b*) A_3 (*c*) A_1 (*d*) A_3

FIGURE 5. Streamlines of the steady axisymmetric solutions for (*a*, *b*) $Re = 105$ and $\Gamma = 2.865$; and (*c*, *d*) $Re = 120$ and $\Gamma = 3.070$.

difference in Γ between the two saddle-node bifurcations) increases. In parts (*c*) and (*d*) of figure 5 are plotted streamlines of co-existing A_1 and A_3 states at $Re = 120$ and $\Gamma = 3.070$. At these higher Re however, the A_1 is not stable for all Γ less than the Γ corresponding to the saddle-node bifurcation S_1. In fact, it is unstable to non-axisymmetric modes, leading to three-dimensional rotating wave solutions. These three-dimensional time-periodic states were observed in the experiments of Mullin & Blohm (2001), and we shall describe them in detail in the following subsection. In this subsection, we are interested in determining the saddle-node bifurcation curve S_1 in (Re, Γ)-space. We have done this using our nonlinear solver restricted to an
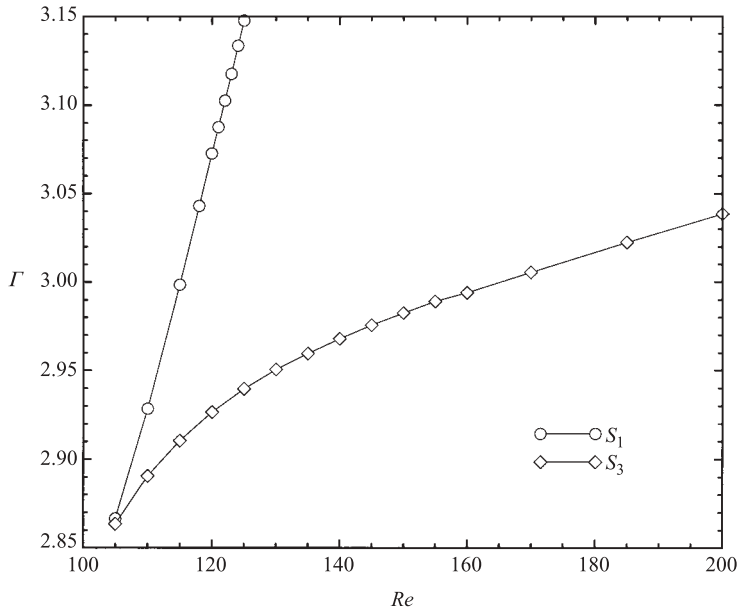
FIGURE 6. Loci of saddle-node bifurcations of the A_1 solutions (labelled S_1) and the A_3 solutions (labelled S_3) in (Re, Γ)-parameter space. They emanate from the codimension-2 cusp bifurcation point.

axisymmetric subspace, in which the A_1 state is stable and exists for Γ up to S_1 (for the range of $Re \in [100, 200]$ considered, the A_3 state is stable where it exists). The loci of S_1 and S_3 are plotted in figure 6. We see that the two saddle-node curves emanate from the codimension-2 cusp point near ($Re \sim 105$, $\Gamma \sim 2.865$). The location of these curves agrees quite well (within one or two percent) with the experimentally and computationally determined curves reported in Mullin & Blohm (2001); compare figures 6 and 1.

3.2. *Supercritical Hopf bifurcations leading to rotating waves*

The experiments of Mullin & Blohm (2001) report interesting three-dimensional time-dependent behaviour as the A_1 state loses stability. They were unable to numerically capture the nonlinear dynamics using their code, which was restricted to solving for steady axisymmetric states. In this subsection, we conduct a comprehensive computational analysis of the three-dimensional time-dependent states that result from the instability of the A_1 state.

The most interesting behaviour reported by Mullin & Blohm (2001) is the presence of a double Hopf bifurcation of A_1. They reported that the two types of Hopf bifurcations, which occur simultaneously at the codimension-2 point, are both supercritical and break the $SO(2)$ symmetry of A_1, but they did not characterize them beyond reporting the frequencies associated with the resulting bifurcated states; they gave no indication of their spatial structure beyond stating that they are three-dimensional. Our computations have determined that the two Hopf bifurcations of A_1 result in rotating waves with azimuthal wavenumbers 1 or 2, denoted RW_1 and RW_2, respectively. Although the azimuthal wavenumbers are in a $1:2$ ratio, the double Hopf bifurcation is non-resonant as the corresponding precession frequencies are incommensurate; the experiments of Mullin & Blohm (2001) also measured the frequencies to be incommensurate in the neighbourhood of the codimension-2 point.
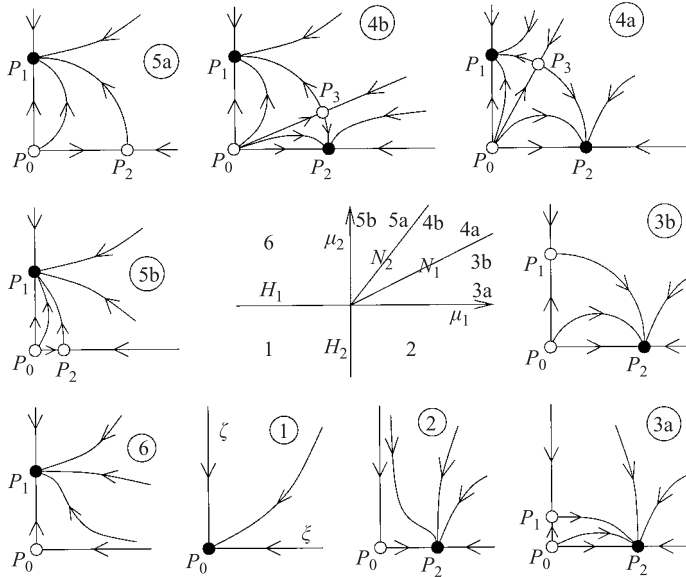
FIGURE 7. Bifurcation diagram of the double Hopf bifurcation, in normal-form variables, corresponding to the present flow. Solid (●) and hollow (○) dots correspond to stable and unstable solutions respectively, μ_1 and μ_2 are the two bifurcation parameters, H_1 and H_2 are the two Hopf bifurcation curves, and N_1 and N_2 are the two Neimark–Sacker bifurcation curves.

So, although we have an $SO(2)$ equivariant system, since there is no resonance at the codimension-2 point, it has the same normal form as the generic (i.e. without symmetry considerations) double Hopf bifurcation (see the detailed discussion on this point in Marques *et al.* 2002). Furthermore, there exists a region of parameter space in the neighbourhood of the codimension-2 point where RW_1 and RW_2 co-exist and are stable. The corresponding normal form in terms of the amplitudes ξ and ζ (of the rotating waves) is

$$\left.\begin{aligned} \dot{\xi} &= \xi(\mu_1 - \xi - \gamma\zeta), \\ \dot{\zeta} &= \zeta(\mu_2 - \delta\xi - \zeta), \end{aligned}\right\} \tag{3.1}$$

plus the trivial equations for the corresponding phases. The values of γ and δ and the relationships between (μ_1, μ_2) and (Γ, Re) corresponding to the double Hopf bifurcation in our flow can be determined from the computed Hopf and Neimark–Sacker bifurcation curves (Hopf bifurcations for limit cycles). The dynamics associated with the normal form (3.1) are shown schematically in figure 7, where the phase portraits are projections onto the (ξ, ζ)-plane, and rotation about each axis recovers phase information. This is the simplest of several possible scenarios, dependent on the values of the normal form coefficients (see Kuznetsov 1998; Marques *et al.* 2002). The origin is a fixed point, P_0, corresponding to the steady axisymmetric base state A_1. The fixed point on the ζ-axis, P_1, corresponds to RW_1 and the fixed point on the ξ-axis, P_2, corresponds to RW_2. The off-axis fixed point, P_3, is an unstable (saddle) two-torus; it is a mixed-mode modulated rotating wave. The parametric portrait in the centre of the figure consists of six distinct regions separated by Hopf bifurcation curves, H_1 and H_2, and Neimark–Sacker bifurcation curves, N_1 and N_2. In region 1, the only fixed point, P_0, is the steady axisymmetric basic state. As μ_1 changes
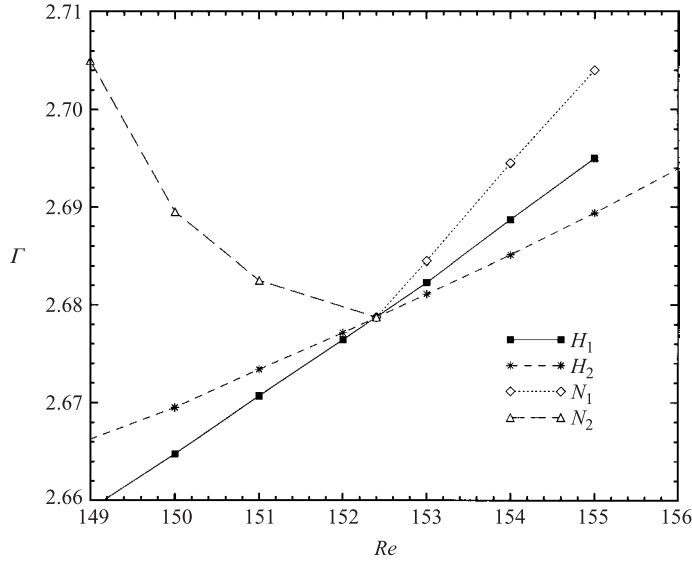
FIGURE 8. Loci in (Re, Γ)-space of Hopf bifurcation curves, H_1 and H_2, from the A_1 flow to rotating waves RW_1 and RW_2, respectively, and Neimark–Sacker bifurcation curves, N_1 and N_2, where the rotating waves lose stability and an unstable mixed mode originates.

sign to positive, P_0 loses stability via a supercritical Hopf bifurcation and a stable rotating wave, P_2, emerges (region 2). When μ_2 becomes positive, P_0 undergoes a second supercritical Hopf bifurcation and an unstable rotating wave, P_1, emerges (region 3). On further parameter variation across the line N_1, the unstable rotating wave undergoes a supercritical Neimark–Sacker bifurcation, becomes stable and an unstable modulated rotating wave, P_3, emerges (region 4). In region 4, there coexist two stable states, P_1 and P_2, and two unstable states, P_0 and P_3. Crossing N_2, P_3 collides with P_2 in another supercritical Neimark–Sacker bifurcation in which the modulated rotating wave vanishes and the rotating wave, P_2, becomes unstable (region 5). On entering region 6, the unstable P_2 collides with the unstable basic state, P_0, in a supercritical Hopf bifurcation and vanishes; P_0 remains unstable. Finally, entering region 1, the stable rotating wave, P_1, collides with P_0, in a supercritical Hopf bifurcation with P_1 vanishing and P_0 becoming stable. The slopes of the N_1 and N_2 curves in terms of the parameters γ and δ in the normal form (3.1) are given by $1/\gamma$ and δ, respectively.

Figure 8 presents the Hopf and Neimark–Sacker bifurcation curves in the neighbourhood of the double Hopf bifurcation; the codimension-2 point is at $(Re = Re_{dH} \approx 152.4,\ \Gamma = \Gamma_{dH} \approx 2.679)$. This is very close to the experimental estimate of the point at $(Re \approx 150,\ \Gamma \approx 2.65)$ (Mullin & Blohm 2001), approximately determined from their figure 7 (reproduced here as figure 1). From the slopes of the tangents to the bifurcation curves in figure 8 at the codimension-2 point, we estimate that $\gamma = 1.528$, $\delta = 1.286$, and that

$$\left.\begin{aligned} \mu_1 &= \Gamma - \Gamma_{dH} - 0.6096(Re - Re_{dH})/Re_{dH}, \\ \mu_2 &= \Gamma - \Gamma_{dH} - 0.8992(Re - Re_{dH})/Re_{dH}. \end{aligned}\right\} \tag{3.2}$$

Some parts of the bifurcation curves are straightforward to compute, but others (such as the unstable parts of H_1 and H_2) require continuation with carefully selected
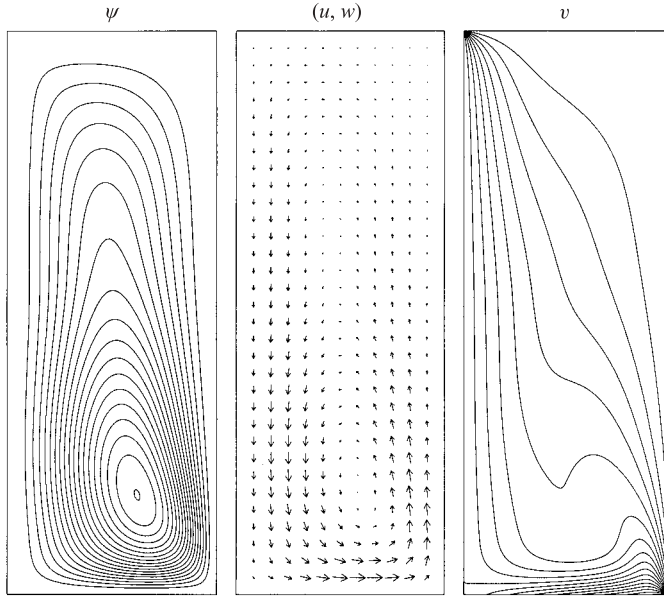
FIGURE 9. Streamlines and velocity components of the unstable A_1 state
at $Re = 150$ and $\Gamma = 2.70$.

initial conditions, and where possible, in selected invariant subspaces (e.g. for H_2, we compute in an even subspace).

To determine H_1 for $Re < 152.5$, one simply computes at fixed Re with increasing Γ until RW_1 states are found. We monitor the solutions by recording the radial velocity at a mid-point of the annulus ($r = (r_o - r_i)/2$, $z = \Gamma/2$, $\theta = 0$), and define the amplitude squared of a rotating wave as the squared difference between the maximum and minimum of the radial velocity at this point over a precession period, denoted as U_1 and U_2 for RW_1 and RW_2, respectively. For a supercritical Hopf bifurcation, the amplitude squared grows linearly with the change in parameter from the bifurcation point; simple linear extrapolation to zero amplitude provides a good estimate of the bifurcation point. The precession frequencies of the rotating waves were also determined from the time records of U_1 and U_2 (near the bifurcation point, frequency variations with parameter variations are of second order). Very near the double Hopf bifurcation point ($Re = 152$, $\Gamma = 2.677$), the computed scaled precession frequency (i.e. the frequency divided by Re) for RW_1 is about 0.079; this compares very well with the experimental estimate of 0.076 from Mullin & Blohm (2001). For RW_2, at ($Re = 152$, $\Gamma = 2.6775$), our numerics give the scaled frequency to be about 0.385. Unfortunately, Mullin & Blohm (2001) do not report the frequency of RW_2 close to the double Hopf bifurcation point, but do indicate that at ($Re \approx 177$, $\Gamma = 2.777$), its scaled frequency is about 0.302; this is also close to our numerically determined value. For $Re = 175$ and $\Gamma = 2.792$, we calculate that the scaled precession frequency of RW_2 is about 0.357.

3.3. Spatial structure of the rotating waves

In the wedge region delineated by the two Neimark–Sacker bifurcation curves, N_1 and N_2, the two rotating wave states are stable. For a point in this region ($Re = 150$, $\Gamma = 2.70$), figure 9 shows the streamlines, ψ, (u, w)-velocity vectors, and contours of azimuthal velocity, v, in a meridional plane for the unstable A_1 state. This state is unstable to both RW_1 and RW_2. Figure 10 presents contours of azimuthal

(a) RW$_1$

(b) RW$_2$

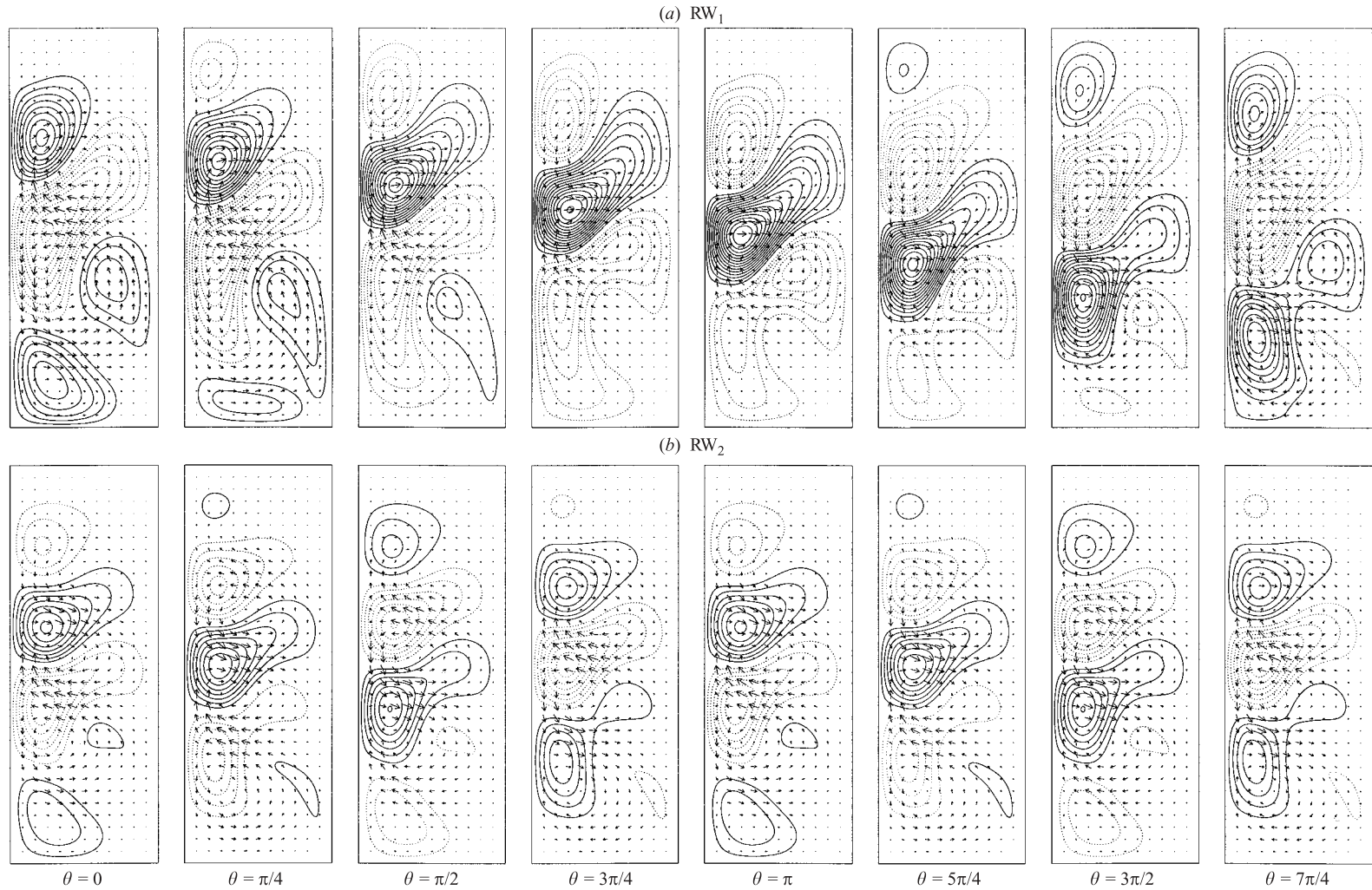| $\theta = 0$ | $\theta = \pi/4$ | $\theta = \pi/2$ | $\theta = 3\pi/4$ | $\theta = \pi$ | $\theta = 5\pi/4$ | $\theta = 3\pi/2$ | $\theta = 7\pi/4$ |

FIGURE 10. Contours of azimuthal velocity together with arrows for the (r, z) components of the $m = 1$ and $m = 2$ Fourier components of the velocity field for (a) RW$_1$ and (b) RW$_2$, respectively, in meridional planes at angles θ as indicated, at $Re = 150$ and $\Gamma = 2.70$.

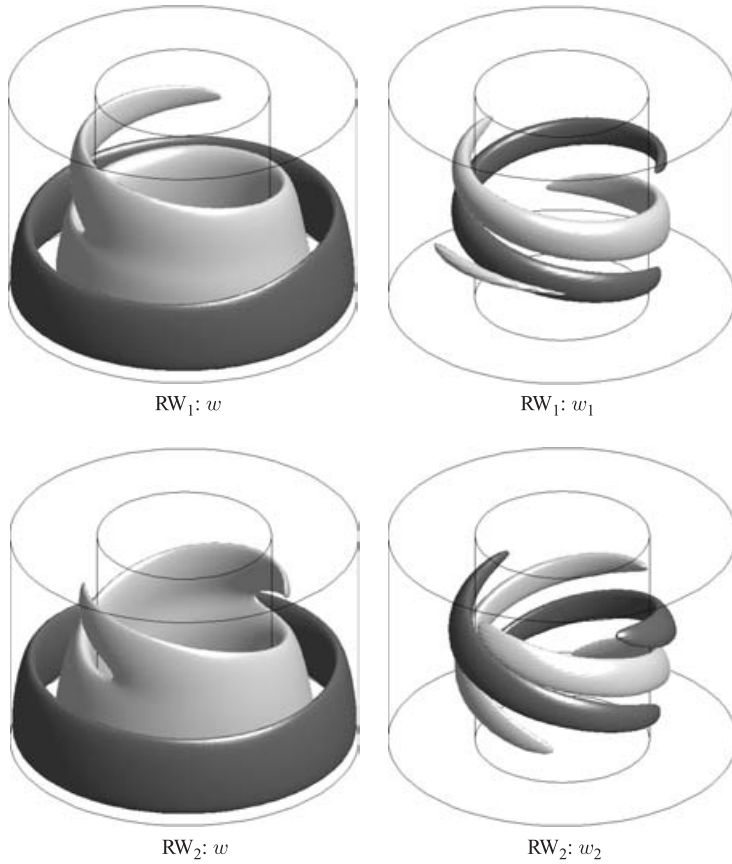RW$_1$: w RW$_1$: w_1

RW$_2$: w RW$_2$: w_2

FIGURE 11. Isosurfaces of the axial component of velocity, w, and the $m = 1$ and $m = 2$ Fourier components of w, w_1 and w_2 respectively for RW$_1$ and RW$_2$ at $Re = 150$ and $\Gamma = 2.70$. The iso-levels shown correspond to half of the maximum positive (light shade) and half of the maximum negative (dark shade) values of w, w_1, and w_2.

velocity together with arrows for the (r, z) components of the $m = 1$ and $m = 2$ Fourier components of the velocity field for RW$_1$ and RW$_2$, respectively, at eight equally spaced meridional planes. The complete velocity fields for RW$_1$ and RW$_2$ essentially correspond to the addition of the A$_1$ state shown in figure 9 to the corresponding Fourier components given in figure 10 (the magnitude of the velocity field corresponding to A$_1$ is about 20 times greater than the magnitude of the Fourier components of either rotating wave at this point in Re and Γ). The single spiral and double spiral nature of RW$_1$ and RW$_2$ is clearly evident in the figure, and more so in the three-dimensional isosurface plots of the axial velocity component and the corresponding Fourier components for RW$_1$ and RW$_2$, shown in figure 11. These Fourier components are the eigenmodes responsible for the Hopf bifurcations from the axisymmetric state shown in figure 9, leading to the rotating waves.

3.4. *Dynamics associated with RW$_1$ for $Re < Re_{dH}$*

Having described locally the two codimension-2 organizing centres for the dynamics over a considerable region of parameter space (i.e. the cusp and double Hopf bifurcations), we now examine more globally how these two interact. Figure 12
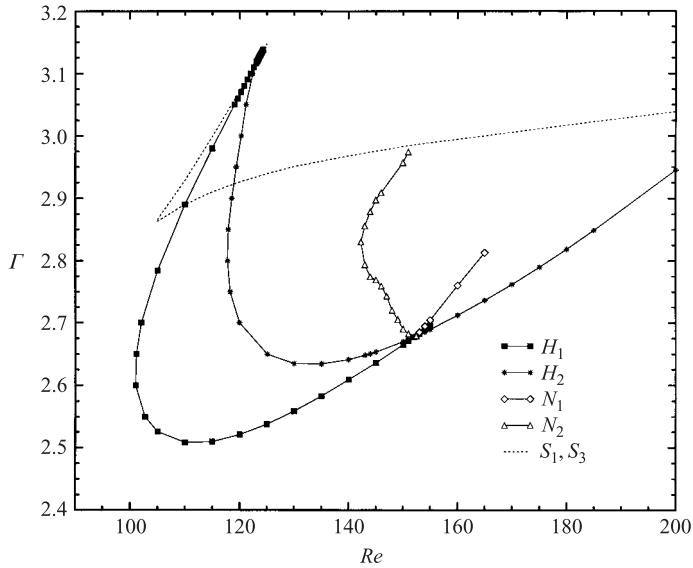
FIGURE 12. Loci in (Re, Γ)-space of Hopf bifurcation curves, H_1 and H_2, from steady axisymmetric single-cell flow to rotating waves RW_1 and RW_2, respectively, Neimark–Sacker bifurcation curves, N_1 and N_2, where the rotating waves lose stability and the unstable mixed mode originates, and the saddle-node bifurcation curves, S_1 and S_3, for the steady A_1 and A_3 states.

gives the locations of the cusp and double Hopf bifurcation points, together with their associated saddle-node, Hopf, and (partial) Neimark–Sacker curves. Overall, the agreement with the corresponding experimentally determined curves by Mullin & Blohm (2001) (figure 1) is very good. Notice however that figure 12 includes an extra curve corresponding to the part of the Hopf bifurcation curve H_2 to the left of the double Hopf bifurcation point. In this region, the RW_2 that results is unstable and cannot be observed directly in the physical experiment. Numerically however, by restricting the computations to an even invariant subspace, this section of H_2 is readily determined.

We now look in more detail at some of the associated dynamics in this region ($Re < Re_{dH}$). Consider the onset of RW_1; this occurs as H_1 is crossed. Figure 13 shows the variation with Γ of the squared amplitude of RW_1 (as measured by U_1), for various fixed values of Re. For small fixed Re (between about 100 and 152), RW_1 is stable at onset and U_1 grows linearly with distance from H_1. For Re greater than about 115, RW_1 loses stability for some range of Γ. The curves in the figure which suddenly stop at finite values of U_1 give an approximate indication of the Γ values, for fixed Re, at which RW_1 becomes unstable via a supercritical Neimark–Sacker bifurcation, resulting in a stable modulated rotating wave, denoted MRW. This modulated rotating wave appears in a region ($Re \gtrsim 115$) far away from the wedge region where the unstable modulated rotating wave associated with the double Hopf bifurcation described earlier exists. Their possible relationship is an open question; to answer it, one needs to compute unstable two-tori, which is beyond the capabilities of our code. At this new Neimark–Sacker bifurcation a new frequency results; MRW has both this frequency and (approximately) the precession frequency of the underlying unstable RW_1. The period associated with this new modulation frequency is denoted T_{MRW}. At onset (i.e. near the Neimark–Sacker bifurcation), T_{MRW}
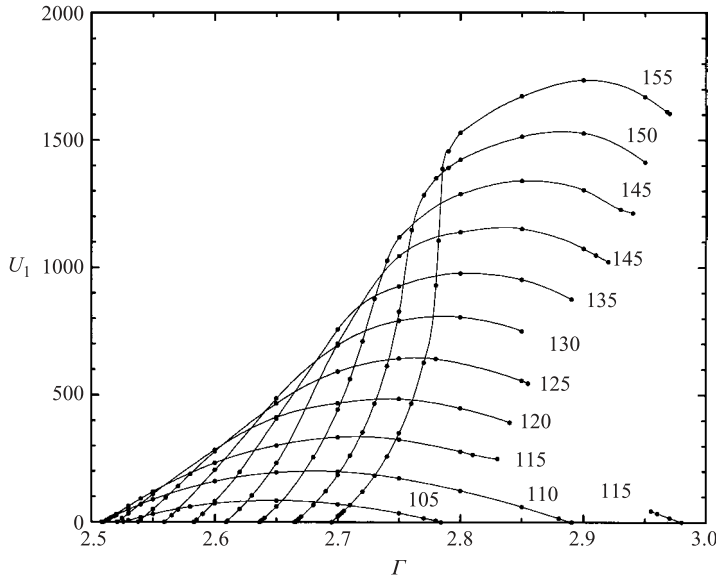
FIGURE 13. Squared amplitude of the centre radial velocity, U_1, for RW_1 versus aspect ratio Γ, for $Re = 105$ to 155 in steps of 5.

is of order one, i.e. of the order of the viscous diffusion time across the annular gap. On moving away from the Neimark–Sacker bifurcation, by increasing Γ, a very rich and complex dynamics unfolds.

In order to explore this complex dynamics in detail, we shall begin by following a one-dimensional path through parameter space, varying Γ while fixing $Re = 120$.

3.5. *One parameter path at $Re = 120$*

In figure 14, the variation of T_{MRW} with Γ (for fixed $Re = 120$) is shown. A number of salient features are immediately obvious from this figure. Most striking is that at two critical values of Γ (approximately 2.969 and 3.0185) $T_{MRW} \to \infty$. The filled circles in the figure are values of T_{MRW} determined from individual computational cases, and the solid lines are logarithmic fits to these data of the form

$$T_{MRW} \sim \frac{1}{\lambda} \ln(1/|\Gamma - \Gamma_c|) + a. \tag{3.3}$$

This behaviour of the period of a cyclic solution is typical as the cycle approaches and becomes homoclinic to a saddle equilibrium at Γ_c as Γ is varied (Gaspard 1990). From these fits, we find good estimates of the Γ-values at which the homoclinic collisions take place; these are 2.96913 and 3.01838. In between these two values of Γ (for fixed $Re = 120$), there are no nearby stable equilibria. In fact, computations attempting to continue solutions into this parameter region invariably evolved to the stable A_3 state. From the ln-fits (3.3), we also obtain very good estimates of λ and a (for the lower-Γ collision, $\lambda = 1.030502$ and $a = -1.75033$, and for the upper-Γ collision, $\lambda = 1.25677$ and $a = -1.61566$); λ is the real part of the eigenvalue corresponding to the unstable manifold of the hyperbolic fixed point (a is simply a fitting parameter with no dynamical significance).

A schematic of the bifurcations for fixed $Re = 120$ and variable Γ is presented in figure 15. For Γ less than 2.521 the only solution is the (stable) A_1, which for larger Γ loses stability via a supercritical Hopf bifurcation (H_1) spawning the stable RW_1.
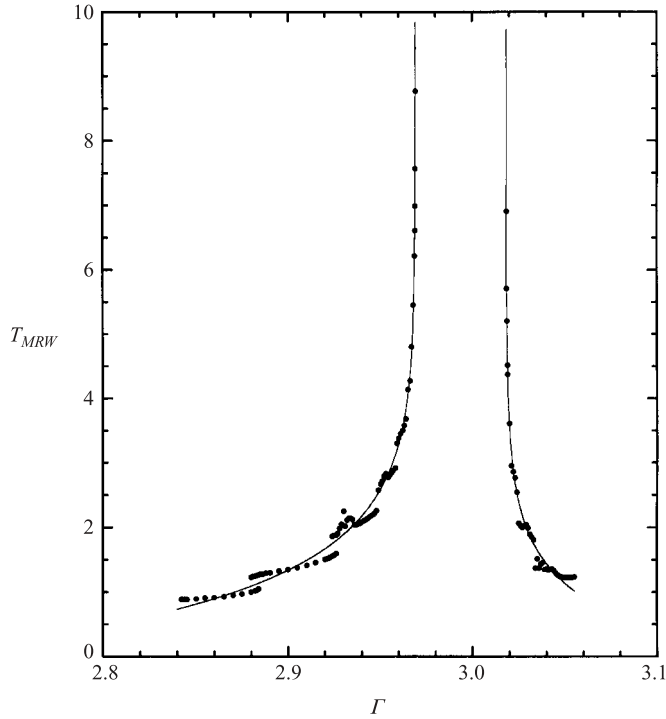
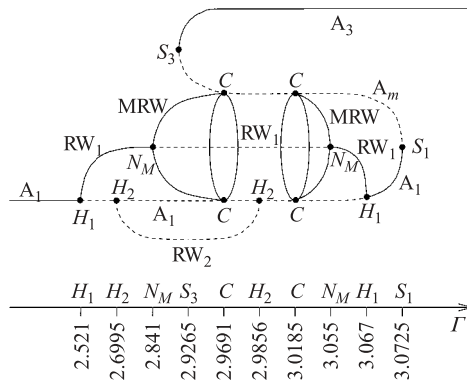FIGURE 14. Modulation period of the MRW solutions for $Re = 120$.

FIGURE 15. Schematic of the bifurcations for $Re = 120$, and varying Γ. Notation for bifurcations: S saddle-node, H Hopf, N Neimark–Sacker, C heteroclinic collision. Notation for the states: A_1, A_3, A_m axisymmetric solutions with one and three cells, and the mid (unstable) saddle solution; RW_i rotating wave with azimuthal wavenumber i; MRW modulated rotating wave (a two-torus). Solid (dashed) lines are (un)stable.

It becomes unstable via a supercritical Neimark–Sacker bifurcation (N_M) at about $\Gamma = 2.841$, spawning in turn the modulated rotating wave MRW. The MRW state undergoes a sequence of saddle-node-type bifurcations as well as some others which have not been clearly identified yet, and finally appears to collide heteroclinically (C) with the saddle A_1 and A_m states at $\Gamma \approx 2.9691$ (this will be discussed in more detail in §3.6). Following the RW_1 state that was spawned at H_1 (at $\Gamma \approx 3.067$) to lower Γ, it also undergoes a supercritical Neimark–Sacker bifurcation (N_M) resulting

in the high-Γ branch of MRW (shown in figure 14). It also undergoes a series of bifurcations and ultimately collides heteroclinically (C) at $\Gamma \approx 3.0185$. For Γ between 2.9691 and 3.0185, the only stable state is the far-off A_3.

At about $\Gamma = 2.6995$, the unstable A_1 state undergoes a second supercritical Hopf bifurcation (H_2) that spawns the (unstable) RW_2 (which we compute in an even subspace); as $\Gamma \to 2.9856$, the amplitude of RW_2 goes to zero at another Hopf bifurcation (note that these two Hopf bifurcations occur on the same Hopf bifurcation curve H_2, see figure 12), with A_1 remaining unstable. At $\Gamma \approx 3.067$ the unstable A_1 undergoes yet another Hopf bifurcation (on the H_1 curve) above which it is stable for larger Γ and a stable MRW is spawned at lower Γ. At $\Gamma \approx 3.0725$, the stable A_1 undergoes a saddle-node bifurcation (S_1) with the (unstable) saddle A_m state, and for larger Γ there are no nearby solutions, only the stable A_3, as shown schematically in figure 15. As the A_3 solution branch is continued to lower Γ, it undergoes a saddle-node bifurcation (S_3) with A_m at $\Gamma \approx 2.9265$, completing the description of the dynamics in this one-dimensional path through parameter space with fixed $Re = 120$.

3.6. *Analysis of the infinite period bifurcation*

Another salient feature is that T_{MRW} does not vary smoothly with Γ. At $\Gamma \approx 2.88$ there is clear evidence of hysteresis, i.e. the multivaluedness of $T_{MRW}(\Gamma)$ in figure 14, from which the presence of saddle-node bifurcations that join stable and unstable tori can be inferred. For the low-Γ portion of this branch, the oscillations associated with the Neimark–Sacker bifurcation from RW_1 leading to the MRW are close to sinusoidal. For the higher Γ portion, the oscillations take on characteristics of a relaxation oscillation, whereby the modal energy in the azimuthal wavenumber $m = 1$ component of the flow, E_1, is asymptotically small over most of the period and then undergoes a rapid excursion during which E_1 grows to large values. The modal energies are

$$E_m = \frac{1}{2} \int_{z=0}^{z=\Gamma} \int_{r=r_i}^{r=r_o} \int_{\theta=0}^{\theta=2\pi} \boldsymbol{u}_m \cdot \bar{\boldsymbol{u}}_m \, r \, \mathrm{d}\theta \, \mathrm{d}r \, \mathrm{d}z. \tag{3.4}$$

There are also other non-smooth features of the variation of T_{MRW} with Γ, particularly for Γ around 2.94 and 3.03, where the solution is not quasi-periodic, but rather irregular in time (in these regimes, figure 14 shows T_{MRW} averaged over several of the irregular cycles); figure 16 shows a selection of E_1 time-series at various Γ values. These features, along with homoclinic/heteroclinic bifurcations, will be better understood in §3.7 within the context of the unfolding of a codimension-2 fold-Hopf bifurcation.

For now, we shall examine in more detail the spatio-temporal structure of MRW. Figure 17 presents contours of the w-velocity minus its $m = 0$ Fourier component, at mid-height $z = \Gamma/2$ for the MRW at $Re = 120$ and $\Gamma = 2.883$, at six different phases during the modulation period $T_{MRW} \approx 1.033$ and figure 18 shows the corresponding temporal variation of E_0 and E_1, the modal energies in the axisymmetric ($m = 0$) and the azimuthal mode 1 ($m = 1$) components of the flow. The modal energy variations are out of phase; the solution exchanges energy between the $m = 0$ and $m = 1$ components of the flow, and the spatial structure of the solution is very similar to that of RW_1 (not drawn here) with the magnitude of the $m = 1$ component essentially being modulated as shown in the time series of E_1. The contour plots in figure 17 are indicative of this; if the flow were a rotating wave these contour plots would be identical but rotated by some angle, and for the MRW solution they have spatial structure (for the field minus the $m = 0$ Fourier component) that essentially does not change (apart
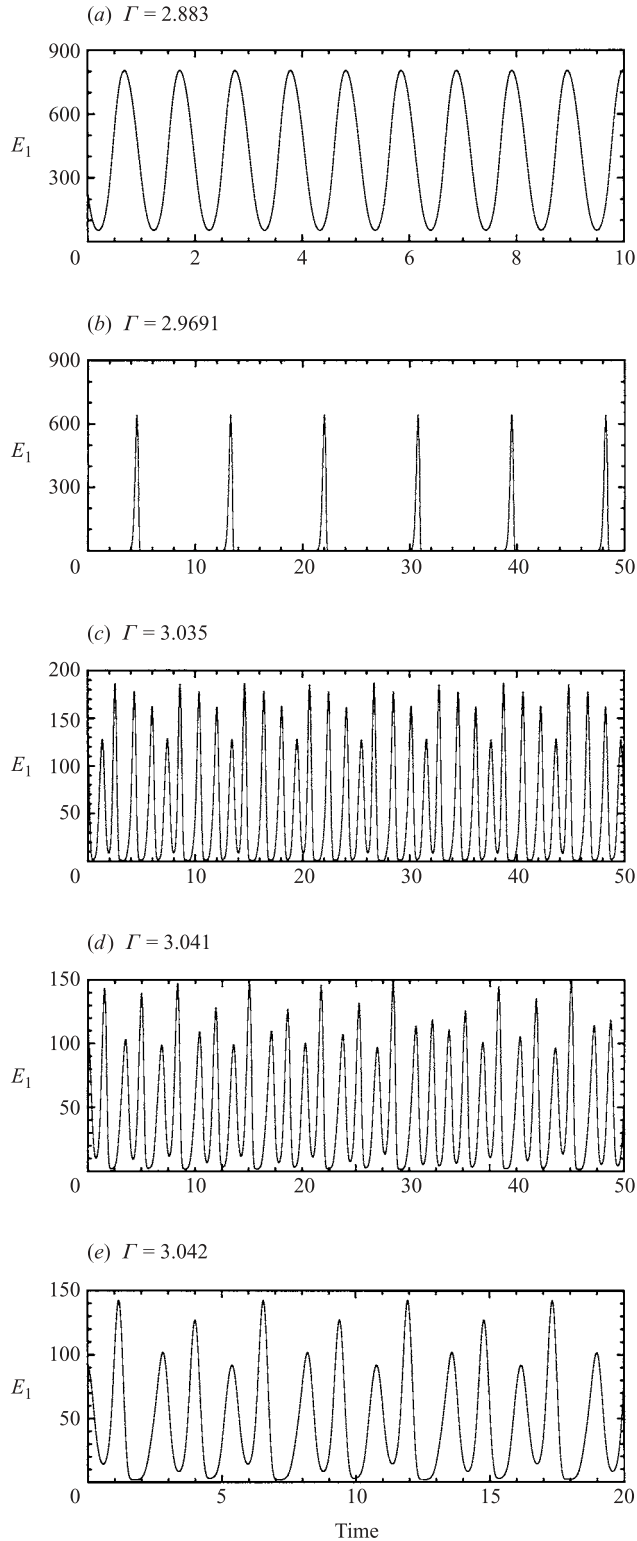
(*a*) $\Gamma = 2.883$

(*b*) $\Gamma = 2.9691$

(*c*) $\Gamma = 3.035$

(*d*) $\Gamma = 3.041$

(*e*) $\Gamma = 3.042$

Time

FIGURE 16. Temporal variation of E_1 for the MRW solutions for $Re = 120$ and Γ as indicated.

(a) $t^* + T_{MRW}/6$ (b) $t^* + 2T_{MRW}/6$ (c) $t^* + 3T_{MRW}/6$

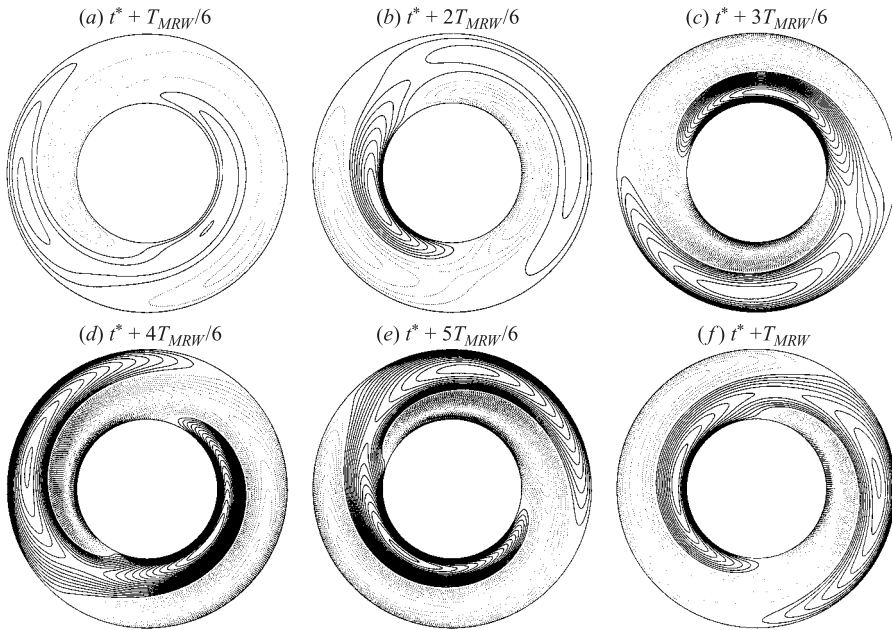(d) $t^* + 4T_{MRW}/6$ (e) $t^* + 5T_{MRW}/6$ (f) $t^* + T_{MRW}$

FIGURE 17. Contours of the w-velocity minus its $m=0$ Fourier component, at mid-height $z = \Gamma/2$ for the MRW at $Re = 120$ and $\Gamma = 2.883$, at six different phases during the modulation period $T_{MRW} \approx 1.033$. Contour levels are kept the same for all phases.
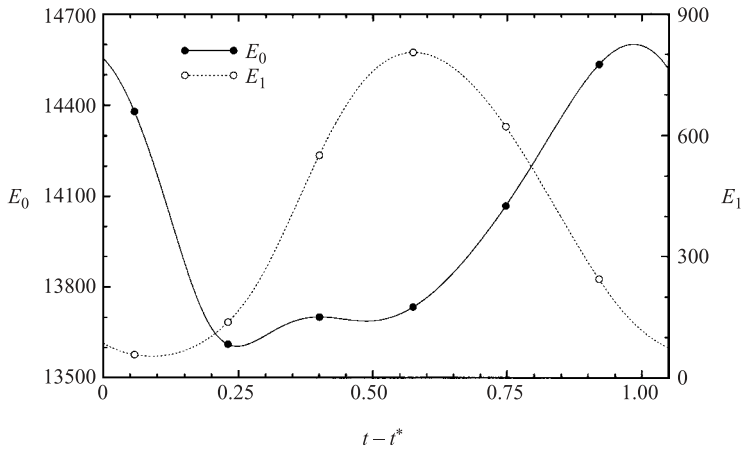

FIGURE 18. Time series of modal energies E_0 and E_1 for MRW at $Re = 120$ and $\Gamma = 2.883$ over approximately one modulation period T_{MRW}. The symbols correspond to the times for the panels in figure 17.

from a rotation), only its magnitude is modulated. Note however that the temporal variations in the modal energies are not harmonic. This becomes more pronounced at higher Γ-values.

Figure 19 shows the temporal variation of E_0 and E_1 for MRW at $Re = 120$ and $\Gamma = 2.969$ where its modulation period is close to becoming unbounded (see figure 14; $T_{MRW} \approx 7.56$ at this point). The modal energy E_1 is essentially zero over most of the modulation period; note that in the figure $\log(E_1)$ is plotted, compare with figure 16b).
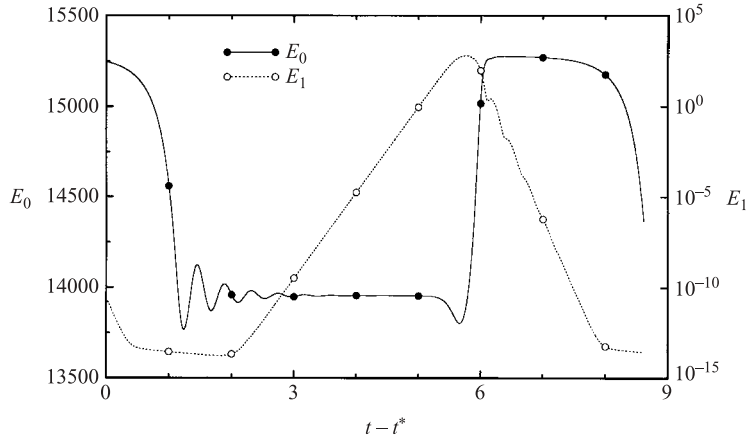
FIGURE 19. Time series of modal energies E_0 and E_1 for MRW at $Re = 120$ and $\Gamma = 2.969$ over approximately one modulation period $T_{MRW} \approx 7.56$. The symbols correspond to the times for the streamline and v-velocity contour plots in figure 20.

This indicates that most of the time, MRW is axisymmetric. The temporal variation of E_0 has features suggestive of a near-heteroclinic cycle; note that for an extensive part of the modulation period (for $t - t^*$ between about 2 and 5), E_0 is approximately constant, and E_1 is very small and growing exponentially. At about $t - t^* = 5$, E_1 saturates and E_0 undergoes a rapid excursion and attains another near-constant value for $t - t^*$ between about 6 and 8, during which time E_1 decays exponentially to very small values. The two rapid excursions in E_0 at times $t - t^*$ approximately 1 and 6 have very distinct characteristics; during the $t - t^* \approx 1$ excursion E_1 is essentially zero so that the near-heteroclinic cycle is essentially residing in an invariant axisymmetric subspace during this time. In contrast, during the $t - t^* \approx 6$ rapid excursion, E_1 is near its maximum value and this part of the near-heteroclinic cycle is far from the axisymmetric subspace. We now examine the spatial structure of MRW over a modulation period to identify the (axisymmetric) hyperbolic fixed points to which the MRW solution is nearly heteroclinic.

The spatial structure of MRW over a modulation period, $T_{MRW} \approx 7.56$, for $Re = 120$ and $\Gamma = 2.969$ is shown in figure 20 in terms of the streamfunction ψ and v-velocity of the axisymmetric component of the solution (note that the flow only has a significant non-axisymmetric component over a very short time interval ($t - t^*$ between about 5.5 and 6). It is evident that for $t - t^*$ between about 2 and 5, MRW is close to an axisymmetric single-cell state. In fact, we have computed the underlying unstable A_1 solution at this same point in parameter space (shown in figure 21a, b) by restricting the computations to the axisymmetric invariant subspace. The plots for MRW of ψ and v in figure 20 (times 2–5) are virtually indistinguishable from the plots of ψ and v for the hyperbolic (unstable) A_1. For times $t - t^*$ between 6 and 8, the MRW has a three-cell structure, but the middle counter-rotating cell is much weaker than the two primary cells near the top and bottom endwall. This structure is quite different to that of the far-off stable A_3 (its ψ and v contours are plotted in figure 21c, d). During this time, we conclude that MRW is close to the (unstable) saddle axisymmetric state A_m, the middle equilibrium in the fold region associated with the cusp bifurcation (see figure 4); its spatial structure is consistent with this, being intermediate between the structure of A_1 and A_3.
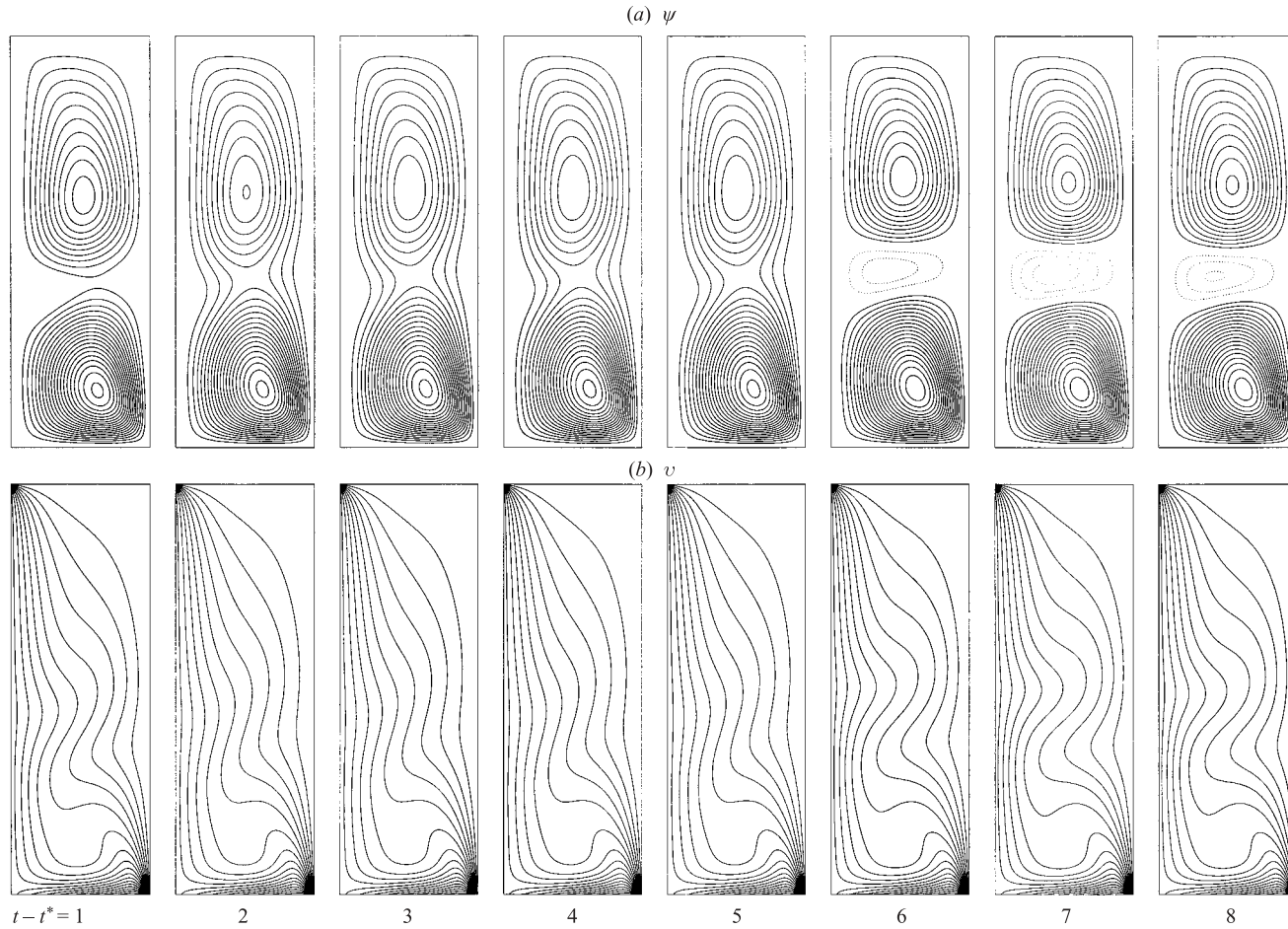
(a) ψ

(b) v

$t - t^* = 1$ 2   3   4   5   6   7   8

FIGURE 20. Contours of (a) the streamlines and (b) v-velocity of MRW (determined using only the $m = 0$ Fourier components of the solution) at eight different phases during the modulation period $T_{MRW} \approx 7.56$ (time indicated is $t - t^*$, corresponding to time axis in figure 19), for $Re = 120$ and $\Gamma = 2.969$.
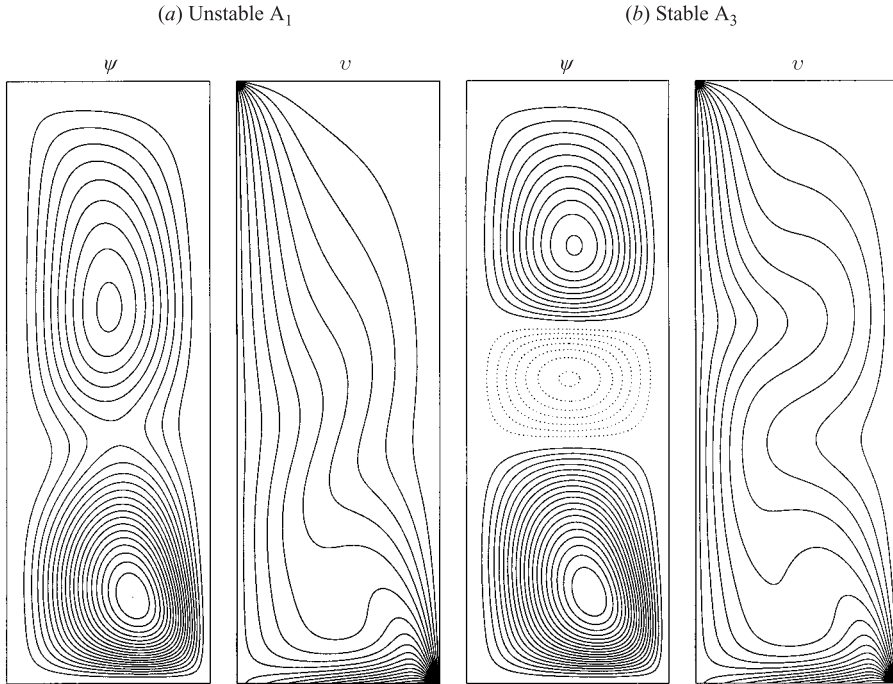
(*a*) Unstable A_1 (*b*) Stable A_3

FIGURE 21. Contours of the streamlines and v-velocity of (*a*) unstable A_1 and (*b*) stable A_3 at $Re = 120$ and $\Gamma = 2.969$.

3.7. *Fold-Hopf bifurcations*

For codimension-1 and some codimension-2 bifurcations, dynamical systems theory provides a *normal form*, a low-dimensional, low-order polynomial system that locally captures the dynamics of the full nonlinear system. Arbitrary perturbations of the normal form result in a topologically equivalent system preserving all the dynamics of the normal form. When the codimension of the system is 2 or greater, persistence of the normal form is not always guaranted. One may still perform a normal-form analysis on the original system, truncating at some finite (low) order and extract some of the characteristic dynamics of the original system; however this formal application of the theory results in a *formal normal form*, with some dynamical features that do not generically persist upon perturbation (e.g. see Kuznetsov 1998). The double Hopf and fold-Hopf bifurcations are typical examples where the dynamics of the formal normal form do not always persist.

We have found in a certain region of the parameter space of our problem that a fold-Hopf bifurcation takes place. Close to this bifurcation, the infinite-dimensional phase space of our problem admits a three-dimensional centre manifold parameterized by a coordinate x, an amplitude ρ and an angle ϕ. The normal form is given by (Kuznetsov 1998)

$$\left.\begin{aligned} \dot{x} &= \mu_1 + x^2 + s\rho^2, \\ \dot{\rho} &= \rho(\mu_2 + \chi x - x^2), \\ \dot{\phi} &= \omega, \end{aligned}\right\} \tag{3.5}$$

where μ_1 and μ_2 are the normalized bifurcation parameters. The eigenvalues at the bifurcation point $\mu_1 = \mu_2 = 0$ are zero and $\pm i\omega$. The coefficients in the normal form
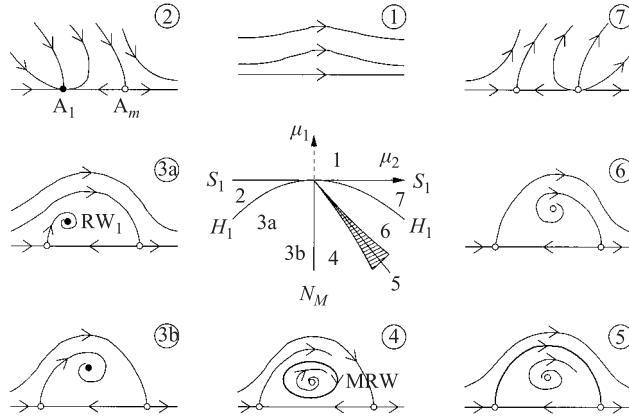
FIGURE 22. Bifurcation diagram of the fold-Hopf bifurcation, in normal-form variables, corresponding to the present flow. Solid ($\bullet$) and hollow ($\circ$) dots correspond to stable and unstable solutions respectively, μ_1 and μ_2 are the two bifurcation parameters, S_1 is a saddle-node bifurcation curve, H_1 is the Hopf bifurcation curve, N_M is the Neimark–Sacker bifurcation curve, and 5 is the horn region of complex dynamics; the straight line inside region 5 is the heteroclinic connection predicted by the formal normal form (3.5) and shown in panel 5.

are $s = \pm 1$, and χ and ω that depend on the parameters μ_1 and μ_2 and satisfy certain non-degeneracy conditions in the neighbourhood of the bifurcation: $\omega \neq 0$, $\chi \neq 0$. The normal form (3.5) admits a multitude of distinct dynamical behaviour, depending on the values of χ and s. These are divided into six distinct bifurcation scenarios. When $s\chi > 0$, only fixed points and a limit cycle exist in the neighbourhood of the bifurcation point. When $s\chi < 0$ more complex solutions exist in the neighbourhood of the fold-Hopf point, including two-tori, heteroclinic structures, homoclinic solutions and more. A comprehensive description of these scenarios is given in Kuznetsov (1998). The different scenarios correspond to $s = \pm 1$, $\chi > 0$ or $\chi < 0$, together with time reversal if necessary (note that only four scenarios are described in Kuznetsov (1998), the other two can be obtained by reversing time when $s\chi < 0$). The fold-Hopf bifurcations present in our problem correspond to these complex cases, and a bifurcation diagram and corresponding phase portraits in the neighbourhood of the fold-Hopf point where S_1 and H_1 coincide are presented in figure 22. We have slightly modified the normal form and plots in Kuznetsov (1998) for a more direct comparison with our representation of the dynamics in (Re, Γ)-parameter space. The normal form (3.5) is generic in the sense that no symmetry considerations were imposed in its derivation. Although our system has $SO(2)$ symmetry, this does not alter the normal form. The only effect of the symmetry is that the bifurcating periodic solution at the Hopf bifurcation is a rotating wave (see Iooss & Adelmeyer 1998).

The fold-Hopf bifurcation resulting from the tangential intersection between S_1 and H_1 in our problem results in complex dynamics (as described above) associated with stable objects (e.g. MRW and its homoclinic collision with either A_1 or A_m) which are directly observable in physical experiments; hence we report these dynamics in detail. The fold-Hopf bifurcation resulting from the tangential intersection between S_1 and H_2 at higher Re and Γ values also results in analogous dynamics which can be computed in the same way, but in an even invariant subspace where the phenomena of interest are stable. However, we do not repeat these rather expensive computations for this case as the results are not directly observable in a physical experiment, as the even subspace is not attainable.
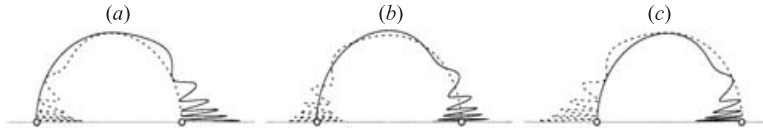
FIGURE 23. Unstable invariant manifold of A_1 (solid) and stable invariant manifold of A_m (dotted): (a) tangency at the beginning of the horn, limiting region 5 in figure 22; (b) transversal intersection inside region 5; (c) tangency at the end of the horn.

The phase portraits in figure 22 are projections onto (x, ρ); rotation about the horizontal axis x recovers angle (ϕ) information. The x-axis is the axisymmetric invariant subspace. The fixed points on the x-axis (A_1 and A_m) correspond to steady axisymmetric states. The off-axis fixed point corresponds to a limit cycle (the rotating wave RW_1). The limit cycle in region 4 is a stable modulated rotating wave (MRW). The parametric portrait in the centre of the figure consists of seven distinct regions separated by different bifurcation curves. Initial conditions starting in region 1 ($\mu_1 > 0$) evolve to far away states, not related to the fold-Hopf bifurcation (in our system, they evolve towards the A_3 steady state). As μ_1 changes sign for $\mu_2 < 0$, the saddle-node bifurcation curve S_1 is crossed, and a pair of fixed points appears: A_1 stable and A_m unstable (region 2). On further decrease of μ_1, the stable fixed point A_1 undergoes a Hopf bifurcation (H_1), becomes unstable and a limit cycle (the rotating wave RW_1) emerges (region 3). Entering region 4, the limit cycle becomes unstable at a Neimark–Sacker bifurcation (N_M), and a stable two-torus (the modulated rotating wave MRW) is born.

If we continue increasing μ_2, according to the analysis of the *formal normal form* (3.5), a heteroclinic invariant two-dimensional manifold appears when MRW collides simultaneously with the two unstable fixed points on the x-axis (the thick line in the phase portrait 5). This occurs along the straight line in the middle of region 5. However, this invariant sphere is a highly degenerate heteroclinic structure and high-order terms in the normal form destroy it (see discussions in Wiggins 1988; Guckenheimer & Holmes 1997; Kuznetsov 1998); in a generic system, instead of a single bifurcation curve associated with this invariant sphere, there is a horn-shaped region about it (the hatched region 5). Generically, the stable invariant manifold of A_m and the unstable invariant manifold of A_1 intersect transversally (while in the formal normal form analysis they coincide). This transversal intersection begins and ends in two heteroclinic tangency curves, the limiting curves of the horn region 5; a schematic of the corresponding phase portraits (replacing panel 5 in figure 22) is presented in figure 23. Inside region 5, the dynamics are extremely complex, including an infinity of two-tori, solutions homoclinic and heteroclinic to both unstable fixed points, cascades of saddle-node and period-doubling bifurcations, and chaos. Figure 24 presents schematic phase portraits of (a) a solution heteroclinic to A_1 and A_m and (b) a solution homoclinic to A_m; a solution homoclinic to A_1 can be obtained from (b) by a reflection. A complete description of the dynamics inside region 5 is still lacking; some effects of higher-order terms in the normal form have been investigated (e.g. see Kirk 1991, 1993). The homoclinic connections presented above are examples of complex Shil'nikov cases that exhibit chaotic dynamics (Wiggins 1988, 1990; Guckenheimer & Holmes 1997; Kuznetsov 1998). This is exactly what we have found in our system, with the MRW solution undergoing several saddle-node bifurcations, their period growing to infinity, and finally disappearing in a homoclinic/heteroclinic collision with either A_1 and/or A_m.
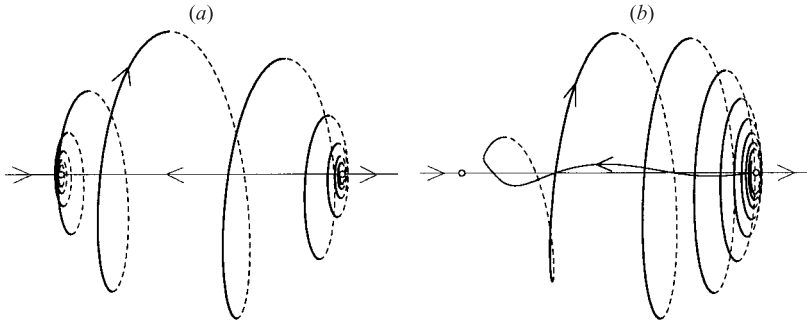
FIGURE 24. Schematics of trajectories (*a*) heteroclinic and (*b*) homoclinic to hyperbolic equilibria that are heteroclinically connected in the invariant subspace (the axis).

Returning to the description of the bifurcation diagram of the fold-Hopf bifurcation in figure 22, on exiting region 5 by a further increase in μ_2, we enter region 6 where the fixed points and limit cycle that exist close to the fold-Hopf bifurcation point are all unstable. Increasing μ_1 and keeping μ_2 constant, the unstable limit cycle RW_1 and A_m merge in a Hopf bifurcation (curve H_1), and we enter region 7 where only the two unstable fixed points A_1 and A_m remain. As μ_1 becomes positive, these two fixed points merge in a saddle-node bifurcation S_1 and disappear; we have returned to region 1 having completed a closed path around the fold-Hopf point in parameter space. Notice that in regions 1, 6, and 7 there are no solutions that remain close to the fold-Hopf point for all times; any solution with initial conditions in any of these three regions evolves towards the remote stable fixed point A_3.

Our numerical simulations of the asymmetric short Taylor–Couette annulus are fully consistent with the above scenario. Recalling figure 15, we can identify all the features of the fold-Hopf bifurcation just described. The one-dimensional parameter path starts with the stable A_1 in region 2, then H_1 is crossed and we are in region 3, where RW_1 is stable. On increasing Γ, N_M is crossed and the stable MRW is born in region 4. Entering region 5, the complex dynamics associated with the horn region appears: MRW undergoes several saddle-node bifurcations, the solutions exhibit complicated temporal behaviour as can be seen in figures 14 and 16, and finally at C MRW undergoes a homoclinic/heteroclinic bifurcation with either A_1 and/or A_m and disappears. In fact, as shown in the schematic phase portraits (figure 24), solutions in a neighbourhood of the homoclinic or heteroclinic connections have trajectories that are very close to both unstable fixed points A_1 and A_m, and so our numerical computations cannot distinguish between the three possible cases of homoclinic/heteroclinic collision for C. In our one-dimensional parameter path there is a range ($\Gamma \in [2.9691, 3.0185]$, for $Re = 120$) where the only stable solution is A_3, corresponding to region 6 (and perhaps region 7). On further increasing Γ, the one-dimensional parameter path takes us back across the bifurcation curves C, N_M and H_1, and we return to the stable steady solution A_1 that undergoes a saddle-node bifurcation with A_m at S_1. We have computed the curves N_M and C for different values of Re and plotted them in figure 25. From this figure, it is clear that the bifurcation curves C, N_M and H_1 are crossed twice along the one-dimensional parameter path with $Re = 120$, described in §3.5, and shown in figure 25 as a grey vertical line at $Re = 120$.

We have not been able to accurately compute a neighbourhood of the codimension-2 fold-Hopf bifurcation point because all the bifurcation curves (S_1, H_1, N_M and C) become almost tangential at the fold-Hopf point. The reason is that the
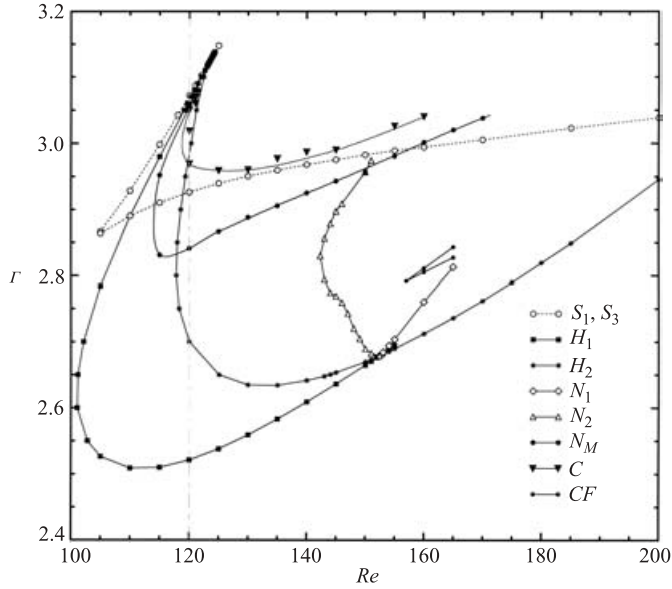
FIGURE 25. Loci in (Re, Γ)-space of the various bifurcation curves described in figure 12, together with the curves of cyclic-folds meeting at a cusp and the Neimark–Sacker curve associate with the fold-Hopf codimension-2 point from H_1 and S_1.

(high-dimensional) manifold of states is projected tangentially onto (Re, Γ)-parameter space due to the fold associated with the saddle-node bifurcation S_1 (see Kuznetsov 1998).

3.8. *Dynamics for $Re > Re_{dH}$*

For $Re > Re_{dH}$ (≈ 152.4), A_1 first loses stability, with increasing Γ, to RW_2 and then to RW_1, so that in this region H_1 is a second Hopf bifurcation of the basic state A_1. Under these circumstances, it is quite difficult to determine the H_1 curve using only a time-evolution code. Nevertheless, near the Hopf bifurcation curves, the growth rates of the critical modes are small, and so using stable RW_1 solutions at nearby (Re, Γ) values as initial conditions, one can transiently evolve towards the unstable RW_1 and determine its amplitude (and precession frequency) before the RW_2 mode grows to significant amplitude. In this manner, we have been able to determine the portion of H_1 shown in figure 8. From these computations, we have determined that H_1 continues to be supercritical for Re a little greater than Re_{dH}. These unstable RW_1 become stable at the Neimark–Sacker bifurcation N_1, shown in figure 25, and plotted in figure 26 are the squared amplitudes, U_1, for these stable RW_1. These curves begin at small but finite U_1 at the Neimark–Sacker bifurcation N_1. As shown in figure 26 for $Re > 155$, there is hysteresis along different portions of the RW_1 branch, e.g. see the U_1 curves for $Re = 160$ and 165. (only the U_1 of the stable RW_1 are drawn). This hysteretic region is bounded by two cyclic-fold bifurcation curves, CF (saddle-node bifurcations for limit cycles). There exists a branch of unstable RW_1 between the two cycle-fold curves. The stable upper branch of RW_1 continues to higher Γ until it loses stability via a Neimark–Sacker bifurcation (N_M) resulting in the MRW state (described earlier for the $Re < Re_{dH}$ cases).

   The pair of cyclic-fold bifurcation curves meet at a codimension-2 cusp point of cyclic-folds, at Re between 155 and 160 and $\Gamma \approx 2.8$. These two bifurcation curves
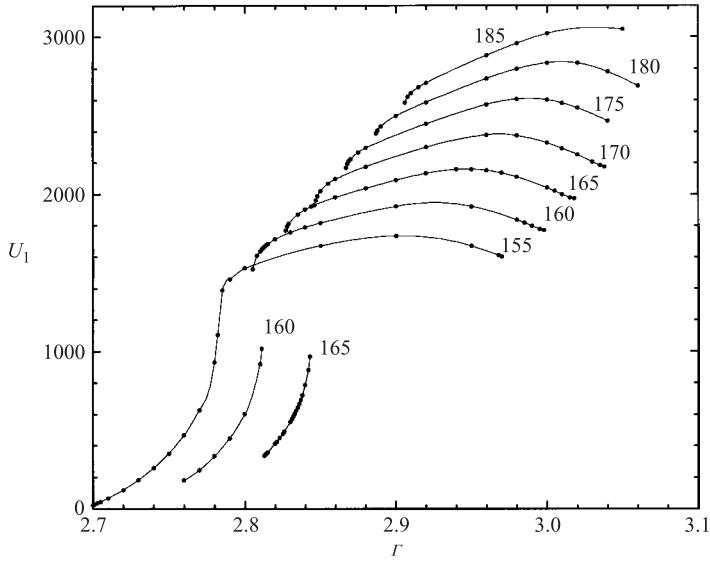
FIGURE 26. Squared amplitude of the centre radial velocity, U_1, for RW$_1$ versus aspect ratio Γ, for $Re = 155$ to 185 in steps of 5.

and the cusp point where they meet are plotted in figure 25 as CF. This figure suggests that there is another codimension-2 point nearby, where the first cyclic-fold curve and N_1 coincide, but no attempt to explore the corresponding dynamics has yet been made. Such a codimension-2 bifurcation point of limit cycles has not yet been studied theoretically (see Kuznetsov 1998, chap. 9).

4. Conclusions

Recent experimental results (Mullin & Blohm 2001) have revealed very interesting dynamics of the flow in a short Taylor–Couette annulus where the top endwall and outer cylinder are stationary and the flow is driven by the constant rotation of the inner cylinder and bottom endwall. This arrangement results in a system with $SO(2)$ as the only symmetry (invariance to rotations about the axis). The dynamics were shown to be organized by a pair of codimension-2 bifurcations: a cusp bifurcation where two curves of (axisymmetric and steady) saddle-node bifurcations meet, and a double Hopf bifurcation where two Hopf bifurcation curves intersect. The Hopf bifurcations were observed to be supercritical and both broke the $SO(2)$ symmetry resulting in three-dimensional time-periodic states. Our computations reproduce all of these dynamics, and further establish that the two Hopf bifurcations result in rotating wave states with azimuthal wavenumbers 1 and 2, respectively. The computed precession frequencies agree very well with the experimentally measured frequencies (obtained using laser Doppler velocimetry at a point). Even the curves of secondary Hopf bifurcations (Neimark–Sacker bifurcations) associated with the double Hopf bifurcation are determined numerically and found to agree very well with the experimentally determined curves.

The numerical computations have also allowed a detailed exploration of the flow dynamics in the fold region associated with the cusp bifurcation. In this region, we have found a pair of fold-Hopf bifurcations (codimension-2 points, where curves of saddle-node and Hopf bifurcations intersect tangentially). At least one of these

is of the complicated type where a Neimark–Sacker bifurcation curve and a thin horn-shaped region of complicated dynamics (involving sequences of saddle-nodes, period-doublings, and heteroclinic and homoclinic collisions) are spawned; a curve of homoclinic/heteroclinic collision between a modulated rotating wave (resulting from the Hopf instability of a rotating wave) and saddle equilibria (either A_1 and/or A_m) in the fold of the cusp bifurcation is determined numerically. All of the associated dynamics are detected numerically, and a detailed bifurcation diagram is obtained that consistently shows the inter-connections between the dynamics associated with the codimension-2 bifurcation points (cusp, double Hopf and fold-Hopf points) and accounts for all the complicated dynamics in a extensive region of parameter space.

REFERENCES

CHORIN, A. J. 1968 Numerical solution of the Navier-Stokes equations. *Math. Comput.* **22**, 745–762.

GASPARD, P. 1990 Measurement of the instability rate of a far-from-equilibrium steady state at an infinite period bifurcation. *J. Phys. Chem.* **94** (1), 1–3.

GUCKENHEIMER, J. & HOLMES, P. 1997 *Nonlinear Oscillations, Dynamical Systems, and Bifurcations of Vector Fields*. Springer.

IOOSS, G. & ADELMEYER, M. 1998 *Topics in Bifurcation Theory and Applications*, 2nd edn. World Scientific.

KIRK, V. 1991 Breaking of symmetry in the saddle-node Hopf bifurcation. *Phys. Lett.* A **154**, 243–248.

KIRK, V. 1993 Merging of resonace tongues. *Physica* D **66**, 267–281.

KUZNETSOV, Y. A. 1998 *Elements of Applied Bifurcation Theory*, 2nd edn. Springer.

LOPEZ, J. M., MARQUES, F. & SHEN, J. 2002 An efficient spectral-projection method for the Navier-Stokes equations in cylindrical geometries II. Three dimensional cases. *J. Comput. Phys.* **176**, 384–401.

LOPEZ, J. M. & SHEN, J. 1998 An efficient spectral-projection method for the Navier-Stokes equations in cylindrical geometries I. Axisymmetric cases. *J. Comput. Phys.* **139**, 308–326.

MARQUES, F., LOPEZ, J. M. & SHEN, J. 2002 Mode interactions in an enclosed swirling flow: a double Hopf bifurcation between azimuthal wavenumbers 0 and 2. *J. Fluid Mech.* **455**, 263–281.

MULLIN, T. & BLOHM, C. 2001 Bifurcation phenomena in a Taylor-Couette flow with asymmetric boundary conditions. *Phys. Fluids* **13**, 136–140.

ORSZAG, S. A. & PATERA, A. T. 1983 Secondary instability of wall-bounded shear flows. *J. Fluid Mech.* **128**, 347–385.

SHEN, J. 1994 Efficient spectral-Galerkin method I. Direct solvers for second- and fourth-order equations by using Legendre polynomials. *SIAM J. Sci. Comput.* **15**, 1489–1505.

SHEN, J. 1997 Efficient spectral-Galerkin methods III. Polar and cylindrical geometries. *SIAM J. Sci. Comput.* **18**, 1583–1604.

TEMAM, R. 1969 Sur l'approximation de la solution des équations de Navier-Stokes par la méthode des pas fractionnaires II. *Arch. Rat. Mech. Anal.* **33**, 377–385.

WIGGINS, S. 1988 *Global Bifurcations and Chaos*. Springer.

WIGGINS, S. 1990 *Introduction to Applied Nonlinear Dynamical Systems and Chaos*. Springer.